

A POPULATION OF DUST-RICH QUASARS AT $Z \sim 1.5$

Y. SOPHIA DAI(戴昱)^{1,2}, JACQUELINE BERGERON³, MARTIN ELVIS¹, ALAIN OMONT³, JIA-SHENG HUANG¹, JAMIE BOCK^{4,5}, ASANTHA COORAY⁶, GIOVANNI FAZIO¹, EVANTHIA HATZIMINAOGLOU⁷, EDO IBAR^{8,9}, GEORGIOS E. MAGDIS^{10,18}, SEB J. OLIVER¹¹, MATHEW J. PAGE¹², ISMAEL PEREZ-FOURNON^{13,14}, DIMITRA RIGOPOULOU^{10,15}, ISAAC G. ROSEBOOM⁹, DOUGLAS SCOTT¹⁶, MYRTO SYMEONIDIS¹², MARKOS TRICHAS¹, JOAQUIN D. VIEIRA⁴, CHRISTOPHER N. A. WILLMER¹⁷, AND MICHAEL ZEMCOV^{4,5}

Draft version September 24, 2018

ABSTRACT

We report *Herschel*¹ SPIRE (250, 350, and 500 μm) detections of 32 quasars with redshifts $0.5 \leq z < 3.6$ from the *Herschel* Multi-tiered Extragalactic Survey (HerMES²). These sources are from a MIPS 24 μm flux-limited sample of 326 quasars in the Lockman Hole Field. The extensive multi-wavelength data available in the field permit construction of the rest-frame Spectral Energy Distributions (SEDs) from ultraviolet to the mid-infrared for all sources, and to the far-infrared (FIR) for the 32 objects. Most quasars with *Herschel* FIR detections show dust temperatures in the range of 25 K to 60 K, with a mean of 34K. The FIR luminosities range from $10^{11.3}$ to $10^{13.5} L_{\odot}$, qualifying most of their hosts as ultra- or hyper-luminous infrared galaxies. These FIR-detected quasars may represent a dust-rich population, but with lower redshifts and fainter luminosities than quasars observed at ~ 1 mm. However, their FIR properties cannot be predicted from shorter wavelengths (0.3–20 μm , rest-frame), and the bolometric luminosities derived using the 5100 \AA index may be underestimated for these FIR-detected quasars. Regardless of redshift, we observed a decline in the relative strength of FIR luminosities for quasars with higher near-infrared luminosities.

Subject headings: galaxies: active, nuclei, starburst – infrared: galaxies – quasars: general

1. INTRODUCTION

The far-infrared (FIR) properties of quasars are critical for our understanding of active galaxy evolution, as they probe

¹ Harvard-Smithsonian Center for Astrophysics, 60 Garden Street, Cambridge, MA 02138, USA; ydai@cfa.harvard.edu

² Boston College, 140 Commonwealth Ave, Chestnut Hill, MA 02468, USA

³ Institut d'Astrophysique de Paris, UMR7095, 98bis boulevard Arago, F-75014, Paris, France

⁴ California Institution of Technology, 1200 East California Blvd, Pasadena CA 91125

⁵ Jet Propulsion Laboratory, 4800 Oak Grove Drive, Pasadena, CA 91109, USA

⁶ Dept. of Physics and Astronomy, University of California, Irvine, CA 92697-4575, USA

⁷ ESO, Karl-Schwarzschild-Str. 2, 85748 Garching bei München, Germany

⁸ UK Astronomy Technology Centre, Royal Observatory, Blackford Hill, Edinburgh EH9 3HJ, UK

⁹ Institute for Astronomy, University of Edinburgh, Royal Observatory, Blackford Hill, Edinburgh EH9 3HJ, UK

¹⁰ Dept. of Astrophysics, Oxford University, Keble Road, Oxford OX1 3RH, UK

¹¹ Astronomy Centre, Department of Physics and Astronomy, University of Sussex, Brighton BN1 9QH

¹² Mullard Space Science Laboratory, University College London, Holm-bury St Mary, Dorking, Surrey RH5 6NT

¹³ Instituto de Astrofísica de Canarias (IAC), E-38200 La Laguna, Tenerife, Spain

¹⁴ Departamento de Astrofísica, Universidad de La Laguna (ULL), E-38205 La Laguna, Tenerife, Spain

¹⁵ Space Science & Technology Dept., Rutherford Appleton Laboratory, Chilton, Didcot, Oxfordshire OX11 0QX, UK

¹⁶ Dept. of Physics and Astronomy, University of British Columbia, Vancouver, B.C., V6T 1Z1, Canada

¹⁷ Steward Observatory, University of Arizona, 933 North Cherry Avenue, Tucson, AZ 85721, USA

¹⁸ CNRS/CEA Saclay, Service d'Astrophysique Orme des Merisiers, F-91191 Gif-sur-Yvette Cedex, France

¹*Herschel* is a ESA space observatory with science instruments provided by European-led Principal Investigator consortia and with important participation from NASA.

²<http://hermes.sussex.ac.uk>

the possible evolutionary connection between star formation and black hole (BH) accretion (e.g. Sanders et al. 1988; Lutz et al. 2007). Both starbursts and active galactic nuclei (AGN) could contribute to the rest-frame FIR emissions at various redshifts, although starbursts are considered to be dominant (e.g. Rowan-Robinson 1995; Trichas et al. 2009). Other models have successfully explained FIR luminosity as originating from direct AGN heating, where cool dust at large distances from the AGN reside in a warped disk/torus (e.g. Sanders et al. 1989; Haas et al. 2003). Spectral information can be used to break this degeneracy. Polycyclic Aromatic Hydrocarbon (PAH) features, for instance, are used to indicate star formation activity (e.g. Lutz et al. 2007). *Spitzer* spectroscopic studies detected PAH emission in some of the Palomar-Green (PG) and Sloan Digital Sky Survey (SDSS) quasars, where strong star formation coexists with quasars, and is responsible for an average of 60% of the FIR emission (e.g. Hao et al. 2005; Netzer et al. 2007; Lutz et al. 2008; Veilleux et al. 2009; Shi et al. 2009).

Rest-frame FIR SED studies provide powerful constraints on the star formation in quasars. Despite large dispersions at different wavelengths for optically bright, unobscured quasars, their mean SEDs show surprising uniformity over redshift, luminosity, and Eddington ratio (e.g. Elvis et al. 1994, hereafter E94; Richards et al. 2006, hereafter R06; Hao et al. 2011). However, the SEDs at rest-frame $\lambda > 40 \mu\text{m}$ were poorly defined at high redshifts (IRAS 100 μm was the longest wavelength for E94 and R06). Several groups have tried to address this FIR gap with various sample selections (e.g. Papovich et al. 2006; Kartaltepe et al. 2010); others have taken advantage of (sub)millimeter observations, e.g., with the Infrared Space Observatory (ISO), the Institut de Radioastronomie Millimétrique (IRAM) telescope, and the Submillimetre Common-User Bolometer Array (SCUBA) (e.g. Omont et al. 2001, 2003; Haas et al. 2003; Priddey et al. 2003a). However, a single photometric point in the rest-frame FIR, as is the case for most (sub)mm quasar

studies, does not strongly constrain the dust temperature distribution for these quasars. The sample sizes for (sub)mm quasars with enough photometric points that allow FIR SED studies, on the other hand, are limited due to the relatively long exposure times required for detections (e.g. Beelen et al. 2006; Wang et al. 2008, 2010). Only about 10 (sub)mm quasars reported to date have detailed rest-frame FIR SED measurements.

The *Herschel* Space Observatory (Pilbratt et al. 2010) has opened a new window (SPIRE: 250, 350, 500 μm , Griffin et al. 2010) to directly study the rest-frame FIR properties for quasars with moderate redshifts ($z \sim 1.5$). The *Herschel* Multi-tiered Extragalactic Survey (HerMES, Oliver et al. 2010; Oliver et al. 2011) covers $\sim 70 \text{ deg}^2$ with rich multi-wavelength data. Along with other *Herschel* surveys, rest-frame 30–300 μm emissions, likely due to cold dust in quasars and other AGNs, have been detected (Hatziminaoglou et al. 2010; Leipski et al. 2010; Serjeant et al. 2010).

In this paper, we report 32 *Herschel* SPIRE detections of 24 μm flux-limited quasars in the HerMES Lockman Hole field. This SPIRE-detected sample constitute at least 10% of the 24 μm selected quasar sample in this field, and allow construction of the complete FIR SEDs for these broad-line quasars at $z \sim 1.5$, which triples the size of (sub)mm observed quasars that have detailed FIR SEDs. Throughout the paper, we assume a concordance cosmology with $H_0=70 \text{ km/s/Mpc}^{-1}$, $\Omega_M=0.3$, and $\Omega_\Lambda=0.7$.

2. MIPS 24 μm -SELECTED QUASARS AND THEIR FIR COUNTERPARTS

The quasars used in this paper are from a 24 μm flux-limited sample in the *Spitzer* Wide-area InfraRed Extragalactic Survey (SWIRE; Lonsdale et al. 2003). In the Lockman Hole–SWIRE (LHS) field, we selected targets that satisfy MIPS $S_{24} > 0.4 \text{ mJy}$ ($\sim 8\sigma$), and 94% of the flux-limited sample also satisfy SDSS $r_{\text{AB}} < 22.5$. In 2009, Huang et al (in prep.) performed a spectroscopic survey of ~ 3000 such 24 μm targets with HECTOSPEC (Fabricant et al. 2005) on the Multiple Mirror Telescope (MMT), with an effective coverage of $\sim 8 \text{ deg}^2$. 93% of these objects have reliable redshifts. SDSS objects with existing spectroscopic z (Hatziminaoglou et al. 2008) that satisfy the same flux-limits were later added to the 24 μm flux-limited sample, which increased the spectroscopic completeness to $\sim 70\%$. Broad line quasars were then selected, where MgII or CIV line width has a FWHM $> 1000 \text{ km s}^{-1}$ (Schneider et al. 2007). The final sample of 326 24 μm -selected sources includes 210 MMT and 116 SDSS quasars.

We matched these 326 quasars to the *HerMES* SPIRE cross-identification (XID) catalog (Roseboom et al. 2010). The XID catalog used SWIRE MIPS 24 μm positions to minimize the source blending effects due to large beam sizes (18'' FWHM for SPIRE 250 μm images), and has a completeness of $\sim 80\%$ at $S_{250} = 20 \text{ mJy}$. Among the 326 24 μm -selected quasars, there are 41 SPIRE detections with $S/N > 5$, of which three were detected at 350 or 500 μm only. We dropped four sources whose SPIRE 250 μm beam covers two 24 μm counterparts (e.g. Fig. 1, bottom). We also excluded the five $z < 0.5$ objects because their rest-frame FIR data points do not constrain the SED fitting. The final sample consists of 32 quasars (20 MMT and 12 SDSS objects) at $0.50 \leq z \leq 3.54$, with a median z of 1.55 (Fig. 2, inset). This corresponds to a 10% detection rate. Since 29 of them were SPIRE 250 μm de-

tected, the 32 quasars used in this paper are hereafter referred to as FIR-detected quasars (Fig. 1, top and middle panels). Twenty-seven sources have at least one 350 or 500 μm detection ($> 3\sigma$), and 16 sources also have SWIRE MIPS 70 or 160 μm detections.

3. SPECTRAL ENERGY DISTRIBUTION

We constructed the rest-frame SEDs for the 32 FIR-detected quasars from the UV to the FIR bands. The LHS field was covered by the Galaxy Evolution Explorer (GALEX) in the ultra-violet (*FUV*, *NUV*), SDSS in the optical (u, g, r, i, and z), the UKIRT Infrared Deep Sky Survey (UKIDSS) in the near infrared (NIR; *J,H,K*), and the SWIRE survey in the mid-infrared (IRAC at 3.6, 4.5, 5.8, and 8.0 μm ; MIPS at 24, 70, and 160 μm). A Chandra X-ray survey covered a small fraction of the LHS field (0.7 deg^2), and only one source (LHS-S119) was detected out of the three FIR-detected quasars within that area (Wilkes et al. 2009). Fig. 1 shows the stamp images for two FIR-detected quasars and one poorly matched quasar in the optical and infrared bands.

The rest-frame FIR emissions of these quasars fall in the 30–300 μm region, similar to those of ISO observed PG quasars (Haas et al. 2003) and (sub)mm-detected quasars (e.g. McMahon et al. 1999; Willott et al. 2003; Priddey et al. 2003a,b; Robson et al. 2004; Omont et al. 2001, 2003; Carilli et al. 2001; Beelen et al. 2006; Wang et al. 2007, 2008, 2010). Using the same method as was adopted in Beelen et al. (2006)¹⁹, we derived the dust mass M_d for the FIR-detected quasars. M_d is in the order of 10^8 – $10^9 M_\odot$, similar to that of (sub)mm quasars. These values are 1–2 dex higher than values estimated for the PG quasars. Therefore, these FIR-detected quasars are associated with the (sub)mm detected quasars as a ‘dust-rich quasar’ population (Fig. 2).

In 31 out of the 32 quasars, the rest-frame SEDs exhibit FIR excess over the E94/R06 quasar templates (Sec. 1) by 0.5 to 2.3 dex at 90 μm , with an average of 1.4 dex. This suggests that the contribution from cool dust is present. We compared the mean SEDs for FIR-detected and the much larger sample of undetected quasars (Fig. 3). These mean SEDs were constructed by combining individual rest-frame SEDs. We first converted the flux densities to luminosities for each object. After shifting their bandpasses to the rest frame, we normalized each SED at 1–5 μm to the R06 template. We then populated a grid of points separated by 0.03 in log wavelength and linearly interpolated between the effective detections from the UV to the FIR. The mean luminosities with this gap-repaired photometry were then connected as the average SED (magenta curves). For FIR-undetected objects, their mean SED was compensated in the FIR with the stacked mean fluxes at 250, 350 and 500 μm from the SPIRE images. These values were estimated by first cutting out maps around the MIPS positions for individual sources (interpolation into sub-pixels was allowed for precisely centering), and then measured from the stacked map via a centered point-spread function (PSF) fitting. Errors associated with the mean fluxes were calculated using the bootstrap method. SEDs for both populations resemble the R06/E94 templates in the optical and the NIR, and differ mainly in the FIR: the stacked S_{250} for FIR-undetected sources is $\sim 8 \text{ mJy}$, about 4 times lower than the median S_{250} for FIR-detected quasars (31.1 mJy). UV-optical reddening is common in both populations, being present in $\sim 40\%$ of the

¹⁹ $M_d = S_{\nu_0} D_L^2 / (1+z) k_d(\nu) B(\nu, T_d)$, where $k_d(\nu) = k_0(\nu/\nu_0)^\beta$ is the dust absorption coefficient. Here we used S_{250} , and k_d is from Alton et al. (2004).

FIR-detected quasars. The reddening corrections are complicated (Hao et al. 2005) and beyond the scope of this paper, as we concentrate in the FIR.

3.1. Modeling the FIR quasar SED

For this work, we adopted a T- α - β model from Blain et al. (2003) to estimate the dust temperatures and quasar luminosities. Different from a pure modified blackbody (MBB) model, which uses an exponential thermal function with emissivity index β to account for a single temperature dust component²⁰; in the T- α - β model, a power-law Wien tail ($f_\nu \propto \nu^{-\alpha} B_{\nu,T}$) is introduced to the mid-IR SED to account for the warmer dust components (Fig. 4). This additional term is then matched to the MBB component at a transition point, where the two functions also have equal first order derivatives. This transition wavelength varies from case to case. We adopted $\beta = 2.0$ here (Priddey et al. 2003a)²¹. At shorter wavelengths, we normalized the R06 template to each SED over the 1–5 μm range for reference.

Out of the 32 quasars, four only have a single band rest-frame FIR detection. One (LHS-M020) of the four sources matches well to the R06 template in the optical and near-infrared bands. The quasar with the highest z , LHS-M268, also has an SED that is well described by the R06 template alone (within 0.2 dex in the FIR). So no fit was attempted for these five objects.

We carried out T- α - β fits to the remaining 27 SEDs, of which 9 objects have all three SPIRE detections. Longward of the Lyman break (912 Å), twenty-two quasars are well-defined by the R06 template and a T- α - β fit. All 12 SDSS quasars fall into this category. The remaining five less-well-defined SEDs show a strong stellar bump in the optical-NIR regime, presumably from the host galaxy, while their FIR SEDs are well described by a T- α - β fit. Fig. 4 presents the individual SED for each of the 32 FIR-detected quasars. The plots are labeled with their ID, redshift, fitted dust temperature and α , and follow an α decreasing order to match Table. 1. No host galaxy correction was applied.

3.2. Dust temperatures and luminosities

The fitted dust temperature (T_d) for these 27 quasars has a range of 18 K–80 K, with 87% of the sources in the range of 25–60 K, and a median and mean of 29 K and 34 K (Fig. 6, right). The fitting error for T_d is less than 10% in $\sim 70\%$ of the cases. However, it is worth noting that the T_d derived from T- α - β fit is on average 30% lower than that from a pure modified blackbody fit, where no power-law term is present. The FIR luminosities are similar within 3σ between these two fits.

The fitted α for these 27 sources has a wide range of 0.68 to 2.44 (Table. 1). Starbursts are found to have higher α values than normal star forming galaxies and quasars, as was shown in Blain et al. (2003). Different α values suggest different dust temperature compositions in individual quasar systems, and may be associated with different evolutionary stages: flatter slopes ($\alpha < 1.0$) imply infrared SEDs with relatively stronger warmer dust emissions, likely heated directly

by the quasar; while steeper slopes $\alpha > 2.0$ indicate a colder dust dominant infrared SED, similar to that of star forming galaxies (Fig. 6, left). Majority of the 27 quasars ($\sim 70\%$) has an α value of $1.0 \leq \alpha \leq 2.0$, possibly in a mixed condition between the two extremes.

The FIR luminosities L_{FIR} (40–300 μm) were estimated by integrating over the fitted SEDs, while the total infrared luminosities L_{IR} (8–1000 μm) (Kennicutt 1998) were integrated over the observed SEDs up to the redshifted MIPS 24 μm data, and over the fitted SEDs at longer wavelength. L_{FIR} ranges from $10^{11.3}$ to $10^{13.5} L_\odot$, while L_{IR} has a range of $10^{11.5}$ to $10^{14.3} L_\odot$, qualifying most of their host galaxies as ultra- or hyper-luminous infrared galaxies (ULIRGs, $L_{\text{IR}} > 10^{12} L_\odot$; HyLIRGs, $L_{\text{IR}} > 10^{13} L_\odot$, Sanders & Mirabel 1996): in the 27 quasars with a T- α - β fit, there are 8 ULIRGs and 13 HyLIRGs. Twenty-one of the 27 quasars have $L_{\text{FIR}}/L_{\text{IR}} > 0.2$, and 16 show $L_{\text{FIR}}/L_{\text{IR}} > 0.5$, indicating major contribution from the FIR to the total L_{IR} . For FIR-undetected quasars, this ratio is ~ 0.3 based on their mean SED (Fig. 3). We also estimated the ‘big blue bump’ luminosity, L_{bb} (0.1–0.4 μm), and the near-infrared luminosity, L_{NIR} (2–10 μm), by integrating over the observed SEDs for all quasars. The 2–10 μm range was chosen to minimize the stellar contribution, and to better represent the ‘hot dust bump’ emission likely to be directly heated by the quasar (Wang et al. 2008). These integration ranges can be found in Fig. 3 as shaded regions. The parameters used and derived from the SEDs are summarized in Table. 1 (See also Fig. 6). Errors for T_d , α , L_{FIR} and L_{IR} are fitting errors only. The errors for L_{bb} and L_{NIR} contain only the photometric errors, and are not listed in Table. 1 because of their small values: mostly at the one percent level or less for L_{bb} , and at most a few percent for L_{NIR} .

The FIR-detected and undetected quasars have similar L_{bb} and L_{NIR} values and distributions, with $L_{\text{NIR}} \sim 25\%$ higher for FIR-detected quasars at higher redshifts (Fig. 7, left). The $L_{\text{FIR}}/L_{\text{NIR}}$ ratio, however, shows an obvious excess over the E94 template range especially at $L_{\text{NIR}} \leq 10^{13} L_\odot$ (Fig. 7, right). We also plot the mean $L_{\text{FIR}}/L_{\text{NIR}}$ ratios for FIR-undetected quasars in three L_{NIR} bins. These values were derived from the mean SEDs at each L_{NIR} bin in the $1 < z < 2$ range (covering the mean z of ~ 1.5), assuming $\beta = 2.0$ and $\alpha = 1.6$ (mean for FIR-detected quasars). These SEDs were completed in the FIR using the stacked fluxes from the SPIRE images for the relevant FIR-undetected sources. For comparison, FIR-detected quasars in the same redshift range are marked with a cross in the center.

It is clear that at the same redshift ($1 < z < 2$ in this case) and luminosity bins, FIR-detected quasars have higher $L_{\text{FIR}}/L_{\text{NIR}}$ ratios than FIR-undetected objects, indicating differences in M_d , T_d , or AGN activities. This ratio seems to decrease at higher L_{NIR} regardless of redshift, though the large scatter at $L_{\text{NIR}} < 10^{13} L_\odot$ prevents determination of a tight correlation. The quasars’ FIR properties cannot be predicted from shorter wavelengths, given the similar SED shapes and luminosities between FIR-detected and undetected quasars at optical and near-infrared regions (Fig. 7, left). Considering this similarity and the common UV extinctions, no bolometric luminosity was calculated for the FIR-detected quasars.

4. DISCUSSION

We constructed a sample of 32 quasars ($0.5 \leq z < 3.6$) with *Herschel* SPIRE detections, which triples the size of (sub)mm observed quasars that have detailed FIR SEDs. These FIR-detected quasars, as well as some FIR-undetected quasars in

²⁰ $f_\nu \propto \nu^\beta B_{\nu,T}$, where $B_{\nu,T}$ is the blackbody spectrum.

²¹ A change in β from 2.0 to 1.5 does not significantly ($< 3\sigma$) change the fitted T_d and the L_{FIR} (see also Sec. 3.2). Since real dust may have a temperature distribution, the fitted temperature only applies to the cold dust component defined by the rest-frame FIR data, while the fitted α term indicates the relative strength of warm and hot dust.

our sample (Fig. 3), show broad line features and strong cold dust emissions simultaneously. This is inconsistent with the evolutionary scenario that naked quasars are only seen when the dust has been blown out (e.g. Haas et al. 2003). The dust detected by *Herschel* show temperatures from 18 K to 80 K (§3.2), with 87% of the sources in a range of 25–60 K, similar to local and $z \sim 2$ starburst galaxies and ULIRGs ($20 \text{ K} < T_d < 60 \text{ K}$) (Calzetti et al. 2000; Magdis et al. 2010). The median and mean T_d in our sample are 29 K and 34 K, respectively. Since the FIR emissions for these FIR-detected and the (sub)mm detected quasars (e.g. Omont et al. 2001, 2003; Carilli et al. 2001; Beelen et al. 2006) both fall in the rest-frame 30–300 μm region, we associated these two populations as a ‘dust-rich quasar’ population (Fig. 2). Estimated dust mass confirmed this connection (See also Sec. 3). ISO-detected quasars (Haas et al. 2003) are possibly at the low- z end of this population, though their M_d could be 1–2 dex lower. A common assumption is that the dust-rich quasars are in transition between optically obscured and unobscured quasar phases, but near-infrared/(sub)mm spectroscopy and high resolution images are needed to test this.

The FIR-detected and undetected quasars have similar mean SEDs (Fig. 3), redshift (Fig. 2, inset) and luminosity distributions (Fig. 7, left) at shorter wavelengths (rest-frame 0.3–20 μm). L_{NIR} is $\sim 25\%$ higher for the FIR-detected population, likely affected by their FIR excess. The lack of correlation between properties at the FIR and shorter wavelengths tests the widely used conversion factor of 7 between $L(5100 \text{ \AA})$ and L_{bol} for AGN and quasars (Shemmer et al. 2004). For these FIR-detected broad line quasars ($\sim 10\%$ of the flux-limited sample), if the rest-frame FIR emission is mainly due to quasar heating, this factor should be modified to 9–20 based on the $L_{\text{FIR}}/L_{\text{IR}}$ ratio. Whether this applies to the flux-limited quasar population in general remains to be investigated.

At $1 < z < 2$, the $L_{\text{FIR}}/L_{\text{NIR}}$ ratios for FIR-detected quasars are on average $2\times$ higher than FIR-undetected ones. $L_{\text{FIR}}/L_{\text{NIR}}$ and L_{NIR} seem to be anti-correlated (Fig. 7, right). This trend is also observed for the overall population despite the large scatter at $L_{\text{NIR}} < 10^{13} L_{\odot}$: the relative strength of L_{FIR} — commonly associated with star formation (e.g. Lutz et al. 2007), decreases at higher L_{NIR} , indicator of warm dust partially or mostly heated by AGN. This trend is consistent with the assumption that star formation is suppressed by the presence of a powerful AGN (Hopkins et al. 2006).

Both star forming galaxies and AGNs may contribute to the rest-frame FIR emission at various redshifts. If we attribute the FIR luminosity to star formation²², as was adopted in

²² Eq(4) in Kennicutt (1998): $\text{SFR} (M_{\odot} \text{yr}^{-1}) = 1.7 \times 10^{-10} L_{\text{IR}} (L_{\odot})$. Here we used L_{FIR}^{40-300} instead of L_{IR}^{8-1000} for a more conservative estimate that re-

some previous studies (e.g. Evans et al. 2006; Riechers et al. 2006; Netzer et al. 2007; Wang et al. 2010, 2011), about 40% of the sample will require a star formation rate (SFR) $> 1000 M_{\odot} \text{yr}^{-1}$, similar to that of submillimeter galaxies (e.g. Lutz et al. 2008). However, for the high luminosity end ($L_{\text{NIR}} \geq 3 \times 10^{13} L_{\odot}$, Fig. 7), with only one source, the statistics are insufficient to prove whether there is a similar proportion of starburst dominated quasars, as was found for (sub)mm observed quasars (i.e. $\sim 20\text{-}30\%$, Wang et al. 2008).

On the other hand, for some quasars, the SFR derived from L_{FIR} reaches $5000 M_{\odot} \text{yr}^{-1}$, which is unlikely and probably implies that part of the FIR emission is powered by AGN. In Fig. 7 (right), we found that for the more luminous quasars ($L_{\text{NIR}} > 5 \times 10^{12} L_{\odot}$), the $L_{\text{FIR}}/L_{\text{NIR}}$ ratio falls in the normal quasar range, suggesting pure quasar heating. Resolved CO and PAH emission from NIR/mm spectroscopy and high resolution imaging showing dust distribution will provide a better estimate of the relative contributions from AGN and starbursts for these dust-rich quasars.

This research has made use of data from the HerMES project — a *Herschel* Key Program utilizing Guaranteed Time from the SPIRE instrument team, ESAC scientists and a mission scientist. SPIRE has been developed by a consortium of institutes led by Cardiff Univ. (UK) and including Univ. Lethbridge (Canada); NAOC (China); CEA, LAM (France); IFSI, Univ. Padua (Italy); IAC (Spain); Stockholm Observatory (Sweden); Imperial College London, RAL, UCL-MSSL, UKATC, Univ. Sussex (UK); Caltech, JPL, NHSC, Univ. Colorado (USA). This development has been supported by national funding agencies: CSA (Canada); NAOC (China); CEA, CNES, CNRS (France); ASI (Italy); MCINN (Spain); SNSB (Sweden); STFC and UKSA (UK); and NASA (USA). The HerMES data were accessed through the HeDaM database (<http://hedam.oamp.fr>) operated by CeSAM and hosted by the Laboratoire d’Astrophysique de Marseille. We acknowledge support from the Science and Technology Facilities Council [grant number ST/F002858/1] and [grant number ST/I000976/1]. This work is based partly on observations made with the *Spitzer* Space Telescope and the MMT Observatory, operated by the Jet Propulsion Laboratory, Caltech under a contract with NASA, and the Smithsonian Astrophysical Observatory and the University of Arizona, respectively. Research by Y. S. D is supported by the SAO Predoctoral Fellowship.

Facility: *Herschel* Space Telescope, MMT, *Spitzer* Space Telescope

duces further contamination from the AGN.

REFERENCES

- Alton, P. B., Xilouris, E. M., Misiriotis, A., Dasyra, K. M., & Dumke, M. 2004, *A&A*, 425, 109
- Beelen, A., Cox, P., Benford, D. J., et al. 2006, *ApJ*, 642, 694
- Blain, A. W., Barnard, V. E., & Chapman, S. C. 2003, *MNRAS*, 338, 733
- Carilli, C. L., Bertoldi, F., Rupen, M. P., et al. 2001, *ApJ*, 555, 625
- Calzetti, D., et al. 2000, *ApJ*, 533, 682
- Evans, A. S., et al. 2006, *AJ*, 132, 2398
- Elvis, M., et al. 1994, *ApJS*, 95, 1
- Fabricant, D., et al. 2005, *PASP*, 117, 14111998, *ApJ*, 498, 579
- Granato, G. L., & Danese, L. 1994, *MNRAS*, 268, 235
- Griffin, M. J., et al. 2010, *A&A*, 518, L3
- Haas, M., et al. 2003, *A&A*, 402, 87
- Hatziminaoglou, E., et al. 2008, *MNRAS*, 386, 1252
- Hatziminaoglou, E., et al. 2010, *A&A*, 518, L33
- Hao, L., et al. 2005, *AJ*, 129, 1795
- Hao, H., Elvis, M., Civano, F., & Lawrence, A. 2011, *ApJ*, 733, 108
- Hopkins, et al. 2006, *ApJS*, 163, 1
- Kartalpe, J. S., et al. 2010, *ApJ*, 709, 572
- Kennicutt, R. C., Jr. 1998, *ARA&A*, 36, 189
- Leipski, C., et al. 2010, *A&A*, 518, L34
- Lonsdale, C. J., et al. 2003, *PASP*, 115, 897
- Lutz, D., Sturm, E., Tacconi, L. J., et al. 2007, *ApJ*, 661, L25
- Lutz, D., et al. 2008, *ApJ*, 684, 853
- Magdis, G. E., Elbaz, D., Hwang, H. S., et al. 2010, *MNRAS*, 409, 22
- McMahon, R. G., Priddey, R. S., Omont, A., Snellen, I., & Withington, S. 1999, *MNRAS*, 309, L1

- Netzer, H., et al. 2007, *ApJ*, 666, 806
 Oliver, S. J., et al. 2010, *A&A*, 518, L21
 Oliver et al. 2011, *MNRAS*, submitted
 Omont, A., Cox, P., Bertoldi, F., et al. 2001, *A&A*, 374, 371
 Omont, A., Beelen, A., Bertoldi, F., et al. 2003, *A&A*, 398, 857
 Papovich, C., et al., 2006, *AJ*, 132, 231
 Pilbratt, G. L., et al. 2010, *A&A*, 518, L1
 Priddey, R. S., Isaak, K. G., McMahon, R. G., & Omont, A. 2003, *MNRAS*, 339, 1183
 Priddey, R. S., Isaak, K. G., McMahon, R. G., Robson, E. I., & Pearson, C. P. 2003, *MNRAS*, 344, L74
 Richards, G. T., et al. 2006, *ApJS*, 166, 470
 Riechers, D. A., Walter, F., Carilli, C. L., et al. 2006, *ApJ*, 650, 604
 Robson, I., Priddey, R. S., Isaak, K. G., & McMahon, R. G. 2004, *MNRAS*, 351, L29
 Roseboom, I. G., et al. 2010, *MNRAS*, 409, 48
 Rowan-Robinson, M. 1995, *MNRAS*, 272, 737
 Sanders, et al. 1988, *ApJ*, 325, 74
 Sanders, D. B., Phinney, E. S., Neugebauer, G., Soifer, B. T., & Matthews, K. 1989, *ApJ*, 347, 29
 Sanders, D. B., & Mirabel, I. F. 1996, *ARA&A*, 34, 749
 Schneider, D. P., Hall, P. B., Richards, G. T., et al. 2007, *AJ*, 134, 102
 Serjeant, S., et al. 2010, *A&A*, 518, L7
 Shemmer, O., et al. 2004, *ApJ*, 614, 547
 Shi, Y., Rieke, G. H., Ogle, P., Jiang, L., & Diamond-Stanic, A. M. 2009, *ApJ*, 703, 1107
 Trichas, M., Georgakakis, A., Rowan-Robinson, M., et al. 2009, *MNRAS*, 399, 663
 Ohta, K., & Miyaji, T. 2003, *ApJ*, 598, 886
 Veilleux, S., et al. 2009, *ApJS*, 182, 628
 Wang, R., Carilli, C. L., Beelen, A., et al. 2007, *AJ*, 134, 617
 Wang, R., Carilli, C. L., Wagg, J., et al. 2008, *ApJ*, 687, 848
 Wang, R., Carilli, C. L., Neri, R., et al. 2010, *ApJ*, 714, 699
 Wang, R., Wagg, J., Carilli, C. L., et al. 2011, *AJ*, 142, 101
 Wilkes, B. J., et al. 2009, *ApJS*, 185, 433
 Willott, C. J., Rawlings, S., & Grimes, J. A. 2003, *ApJ*, 598, 909

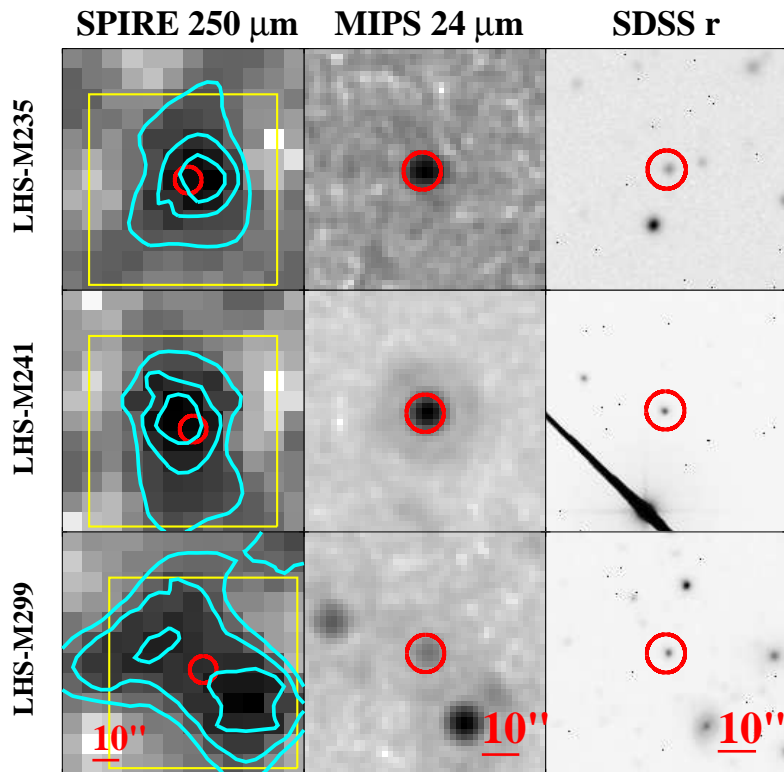


FIG. 1.— Multi-wavelength images for two FIR-detected (top and middle) and one confused (bottom) quasars. The red circles in all three bands indicate the optical positions and have a $5''$ radius. The sizes of the optical-mid-IR images are $50'' \times 50''$, corresponding to the yellow squares in the $250 \mu\text{m}$ images. The cyan contours in the $250 \mu\text{m}$ image mark the $3, 6, \text{ and } 9 \times \sigma$. The FIR emission corresponds to an isolated $24 \mu\text{m}$ source in all the 32 FIR-detected quasars listed in Table. 1. The bottom panel shows one of the four confusing cases excluded from the 41 sources with 5σ SPIRE signal.

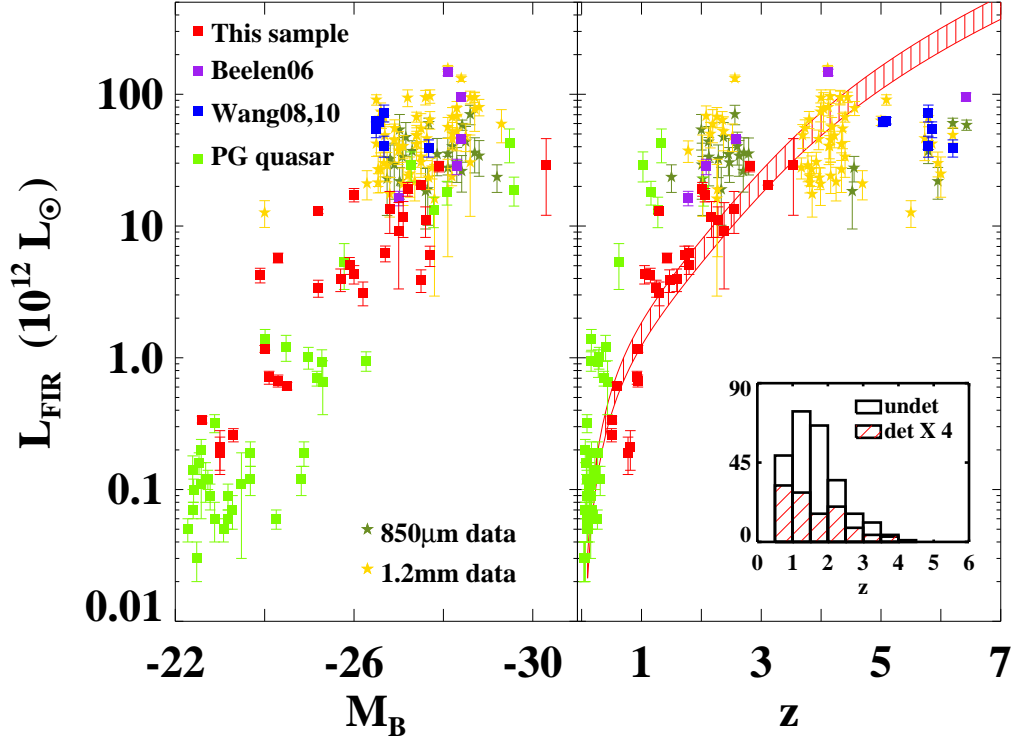


FIG. 2.— Relation between the FIR luminosities and absolute B band magnitudes (left panel), and redshifts (right panel) for *Herschel* FIR-detected quasars (red), ISO-detected PG quasars (green), and (sub)mm-detected quasars — olive and yellow stars for quasars with single band (sub)mm photometry, purple and blue squares for those with multi-band (sub)mm data (for references, see Sec. 3). L_{FIR} was estimated with a $T\text{-}\alpha\text{-}\beta$ method for all sources (Sec. 3.1). The shaded area in red plots the SPIRE selection function at $S_{250} = 20$ mJy, and the range results from the assumed 20% flux error (5σ). This selection function was derived using fixed $\alpha = 1.6$ and $T_d = 34K$ (mean values of the 27 objects with a $T\text{-}\alpha\text{-}\beta$ fit). Some sources are below the SPIRE selection region due to lower T_d or higher α . For objects with only one photometric point ($850\mu\text{m}$ or 1.2mm data), we adopted for the fit $\alpha = 1.6$, and $T_d = 43K$ — mean values for (sub)mm quasars with multi-wavelength data (Beelen et al. 2006; Wang et al. 2008, 2010). The inset shows the redshift distribution for the FIR-undetected quasars in our sample, with the 32 FIR-detected quasars in red hatching and scaled by $4\times$ for comparison.

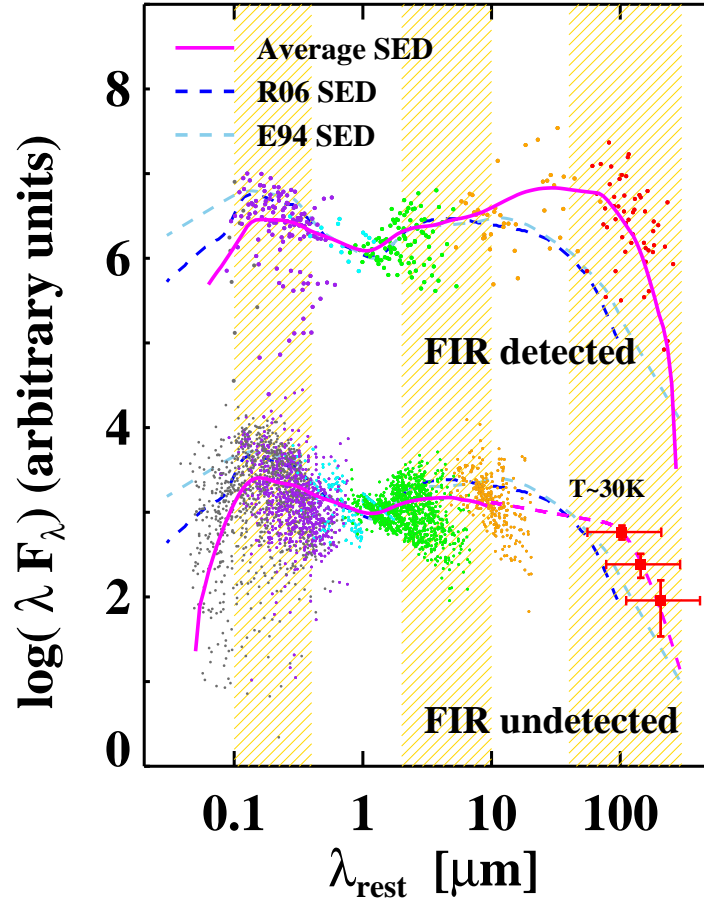


FIG. 3.— Rest-frame mean SEDs for FIR-detected and undetected quasars (arbitrary units). The colored dots show the detections (normalized to R06 template at $1\text{--}5\ \mu\text{m}$): *grey*, GALEX; *purple*, SDSS; *cyan*, UKIDSS; *green*, SWIRE-IRAC; *orange*, SWIRE-MIPS; *red*, HerMES-SPIRE. In magenta are the mean SEDs for FIR-detected and undetected quasars derived from these normalized detections (see Sec. 3). Dashed curves in dark and light blue mark the relative positions of the E94 and R06 templates (normalized at $1\ \mu\text{m}$). For FIR-undetected quasars, the stacked mean fluxes from the SPIRE images are plotted as red squares, shifted to the rest-frame assuming $z = 1.5$ (mean for FIR-undetected objects), and errors in the x-axis show the redshift span of $0.2 \sim 4.0$. The regions used for L_{bb} , L_{NIR} , and L_{FIR} integration are shaded in yellow.

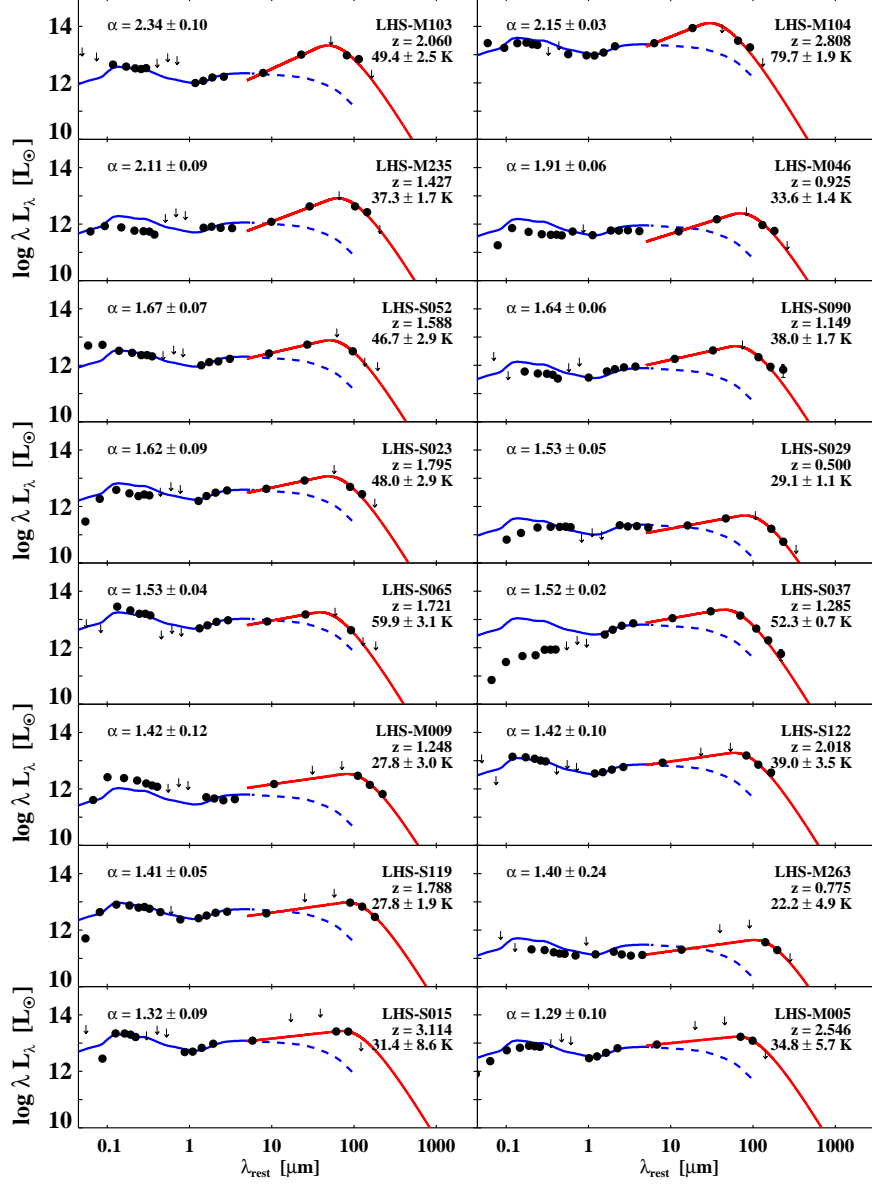


FIG. 4.— Individual rest-frame SEDs for the FIR-detected quasars in our sample, with energy λL_λ in L_\odot . The SEDs were constructed with existing data from the UV to the mid-infrared, complemented in the FIR by the HerMES-SPIRE observations (see Fig. 3 for details). The red curves plot a T - α - β fit with $\beta = 2.0$, with fitted T_d and α given in the legend, and blue curves are the R06 template normalized at 1–5 μm . The parameters are summarized in Table. 1. The objects are arranged in an α decreasing order, and followed by quasars with special SED shapes. No host galaxy correction was applied.

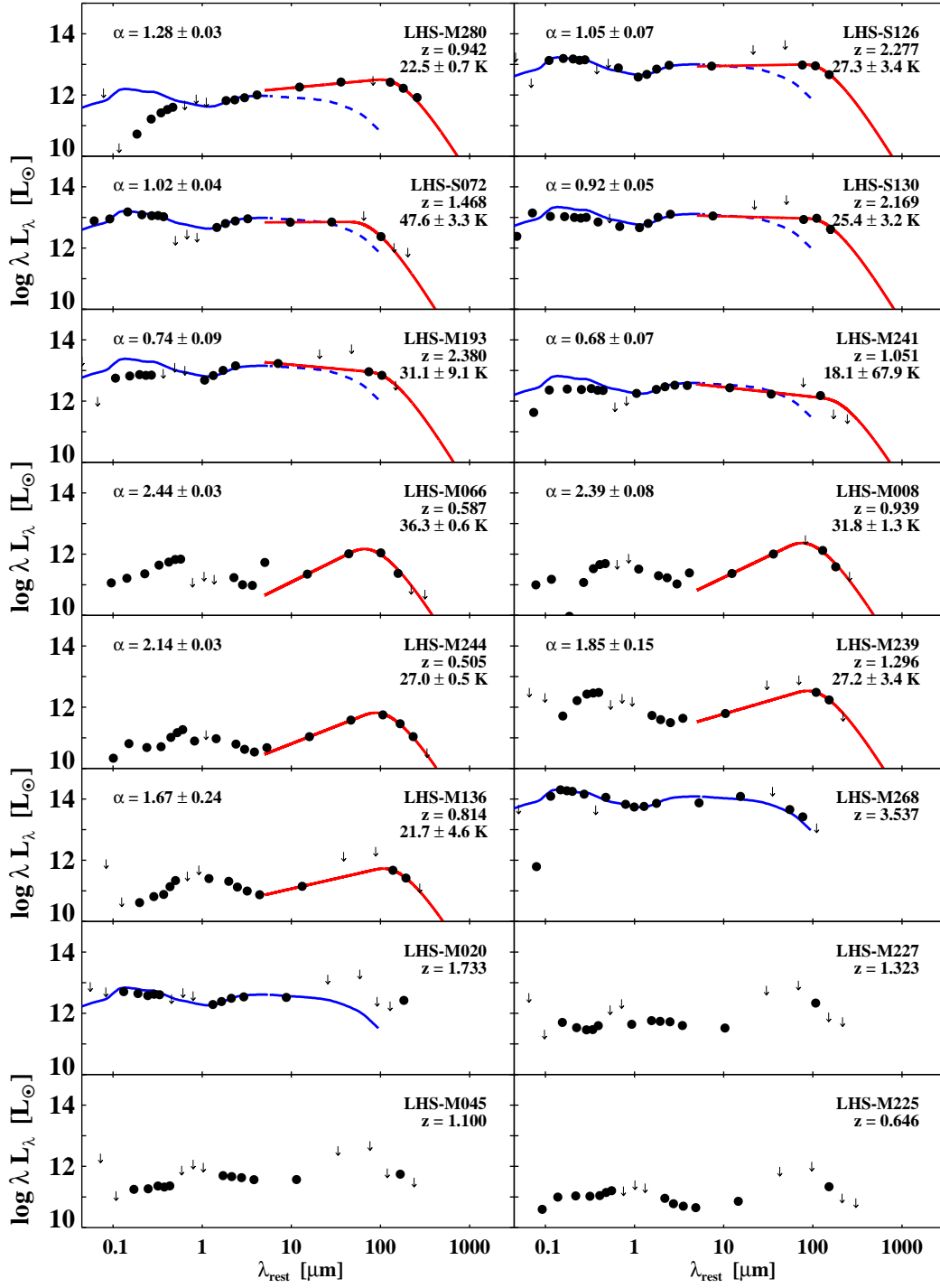


FIG. 5.— Fig. 4, Continued.

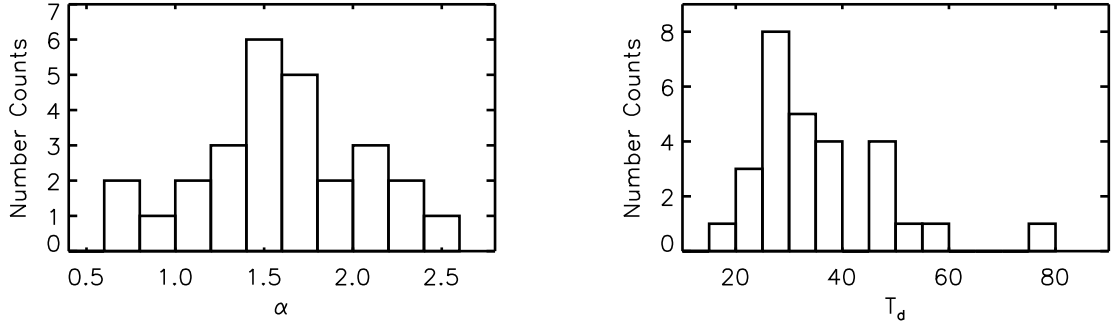


FIG. 6.— Histograms of the fitted power-law slope α (left) and the dust temperature T_d (right) for the FIR-detected quasars.

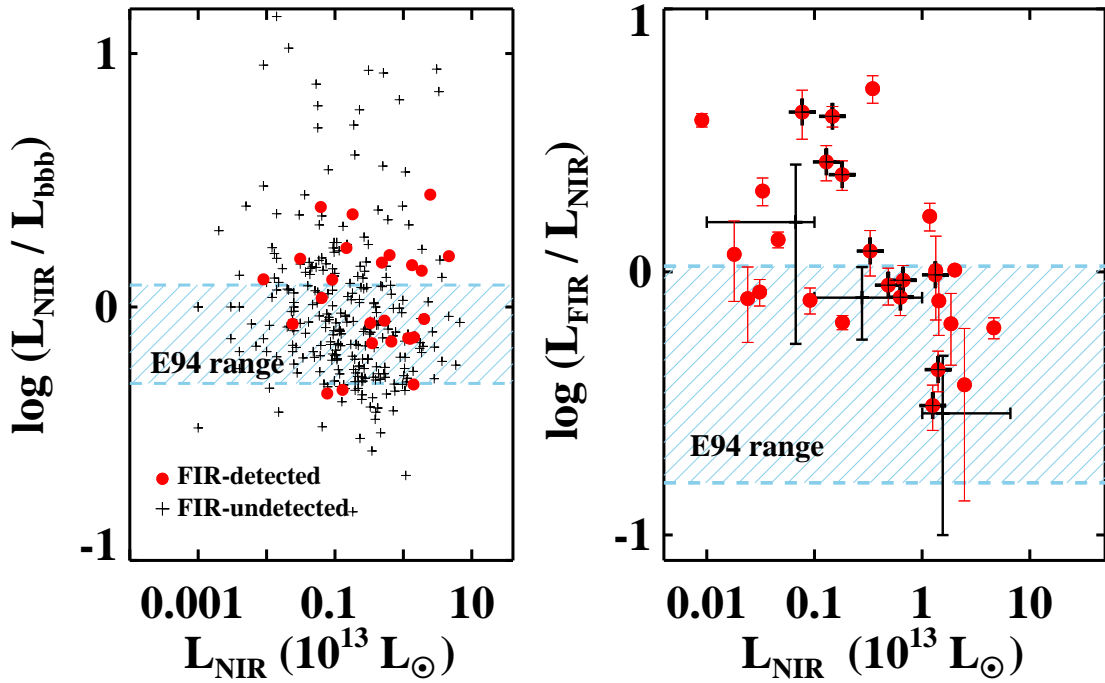


FIG. 7.— (left) Ratio between the near-infrared and the ‘big blue bump’ luminosities (definitions in Sec. 3.2 and Fig. 4, left). Hatched area marks the E94 predicted range (90% confidence, E94 was used since R06 template stops at rest-frame $100 \mu\text{m}$). (right) The relation between FIR and NIR luminosities for FIR-detected quasars. Eleven FIR-detected sources have a higher ratio than the E94 prediction. Significant higher $L_{\text{FIR}}/L_{\text{NIR}}$ ratios are observed at $L_{\text{NIR}} \leq 10^{13} L_{\odot}$, whereas more luminous quasars ($L_{\text{NIR}} > 10^{13} L_{\odot}$) show relatively weaker FIR dust emission. Large black crosses are the mean $L_{\text{FIR}}/L_{\text{NIR}}$ ratios for FIR-undetected quasars at $1 < z < 2$ in each L_{NIR} bin. FIR-detected quasars of the same redshift range are marked with a small cross at the center.

TABLE 1
PARAMETERS DERIVED FROM THE FITTED SED.

Object ID	z	T_d (K)	α	$L_{\text{bb}}^{0.1-0.4\mu\text{m}}$ ($10^{12}L_\odot$)	$L_{\text{NIR}}^{2-10\mu\text{m}}$ ($10^{12}L_\odot$)	$L_{\text{FIR}}^{40-300\mu\text{m}}$ ($10^{12}L_\odot$)	$L_{\text{IR}}^{8-1000\mu\text{m}}$ ($10^{12}L_\odot$)	SFR (M_\odot/yr)	$\log M_d$ (M_\odot)
(1)	(2)	(3)	(4)	(5)	(6)	(7)	(8)	(9)	(10)
LHS-M103	2.060	49.4±2.5	2.34±0.10	4.82	3.47	17.26±2.01	31.00±3.61	3000	8.9
LHS-M104	2.808	79.7±1.9	2.15±0.03	29.18	46.30	28.38±2.59	115.84±10.56	5000	8.9
LHS-M235	1.427	37.3±1.7	2.11±0.09	0.86	1.47	5.74±0.49	8.68±0.74	1000	9.1
LHS-M046	0.925	33.6±1.4	1.91±0.06	0.71	0.91	0.71±0.08	1.05±0.12	100	9.4
LHS-S052	1.588	46.7±2.9	1.67±0.07	3.81	3.29	3.95±0.77	8.00±1.57	700	8.6
LHS-S090	1.149	38.0±1.7	1.64±0.06	0.78	1.81	4.24±0.54	7.29±0.93	700	8.7
LHS-S023	1.795	48.0±2.9	1.62±0.09	3.92	6.28	5.03±0.74	10.82±1.60	900	9.5
LHS-S029	0.500	29.1±1.1	1.53±0.05	0.20	0.31	0.26±0.03	0.39±0.04	40	8.7
LHS-S065	1.721	59.9±3.1	1.53±0.04	28.45	14.07	5.98±1.05	16.93±2.97	1000	8.5
LHS-S037	1.285	52.3±0.7	1.52±0.02	0.81	13.26	12.92±0.50	29.86±1.15	2200	8.2
LHS-M009	1.248	27.8±3.0	1.42±0.12	2.74	1.29	3.38±0.50	5.69±0.84	600	9.1
LHS-S122	2.018	39.0±3.5	1.42±0.10	15.60	11.76	19.14±2.30	39.32±4.73	3300	9.3
LHS-S119	1.788	27.8±1.9	1.41±0.05	9.13	6.67	6.20±0.85	10.94±1.49	1100	9.4
LHS-M263	0.775	22.2±4.9	1.40±0.24	0.28	0.24	0.19±0.06	0.30±0.09	30	8.6
LHS-S015	3.114	31.4±8.6	1.32±0.09	22.42	20.10	30.16±21.82	58.81±42.55	3500	8.7
LHS-M005	2.546	34.8±5.7	1.29±0.10	9.15	13.38	13.54±4.75	27.99±9.82	2300	8.8
LHS-M280	0.942	22.5±0.7	1.28±0.03	0.09	1.82	1.17±0.07	1.97±0.12	200	8.5
LHS-S126	2.277	27.3±3.4	1.05±0.07	18.82	14.29	11.09±2.89	24.44±6.37	1900	9.3
LHS-S072	1.468	47.6±3.3	1.02±0.04	16.73	12.53	3.89±0.76	10.66±2.08	700	8.5
LHS-S130	2.169	25.4±3.2	0.92±0.05	13.33	18.53	11.77±3.58	28.01±8.51	2000	9.4
LHS-M193	2.380	31.1±9.1	0.74±0.09	8.91	24.72	9.20±5.87	26.93±17.20	1600	9.3
LHS-M241	1.051	18.1±67.9	0.68±0.07	3.24	4.85	2.21±22.06	5.21±51.91	400	...
LHS-M066	0.587	36.3±0.6	2.44±0.03	0.36	0.46*	0.61±0.04	0.81±0.05	100	8.1
LHS-M008	0.939	31.8±1.3	2.39±0.08	0.19	0.33*	0.67±0.07	0.89±0.09	100	8.8
LHS-M244	0.505	27.0±0.5	2.14±0.03	0.07	0.09*	0.34±0.02	0.44±0.03	60	9.1
LHS-M239	1.296	27.2±3.4	1.85±0.15	1.69	0.77*	3.12±0.64	4.52±0.92	500	8.9
LHS-M136	0.814	21.7±4.6	1.67±0.24	0.05	0.18*	0.21±0.07	0.31±0.10	40	8.8
LHS-M268†	3.537	208.91	129.92
LHS-M020	1.733	5.99	5.29
LHS-M227	1.323	0.59	0.64*
LHS-M045	1.100	0.25	0.62*
LHS-M225	0.646	0.13	0.09*

NOTE. — (1): Object ID. (2): Spectroscopic redshifts determined from Hectospec and SDSS spectra. (3) (4): Dust temperature and power-law index derived from the T- α - β fit (see also Sec. 3.1). (5) (6) (7) (8): Luminosities estimated from the SED (see also Sec. 3.2). (9): Star formation rate estimated using $L_{\text{FIR}}^{40-300\mu\text{m}}$ following the Kennicutt law (1998), see Sec. 4, footnote. (10): Dust mass calculated using S_{250} , see Sec. 3, footnote.

*: not corrected for host galaxy contamination. †: SED well defined by R06 template, no T- α - β fit needed.